

A Novel Method for Mass Measurement by Quantitative Image Deformation

Xuejun Zhang (✉ xjzhang@gxu.edu.cn)

Guangxi University <https://orcid.org/0000-0001-7689-4686>

Chan Liang

Guangxi University <https://orcid.org/0000-0001-8991-9838>

Huan Lao

Guangxi University

Binmei Liang

Guangxi University

Yinghua Sun

Guangxi University for Nationalities

Research

Keywords: thin plate spline, Fast Fourier Transform, mass, bending energy, image processing

Posted Date: September 3rd, 2020

DOI: <https://doi.org/10.21203/rs.3.rs-67777/v1>

License:   This work is licensed under a Creative Commons Attribution 4.0 International License.

[Read Full License](#)

RESEARCH

A Novel Method for Mass Measurement by Quantitative Image Deformation

Xuejun Zhang^{1,2*}, Chan Liang¹, Huan Lao³, Binmei Liang¹ and Yinghua Sun⁴

*Correspondence:

xjzhang@gxu.edu.cn

¹School of Computer, Electronics and Information, Guangxi University, Nanning, 530004 Guangxi, China

Full list of author information is available at the end of the article

Abstract

Mass of an object is an important characteristic for quality assessment. However, in some cases, it is hard to measure the mass of objects with instruments directly. In this paper, we proposed a novel method based on image processing to measure the mass of an object by analyzing the deformation degree in a grid pattern. In the spatial field, thin plate spline algorithm was adopted to calculate the minimum deformation bending energy in order to give a quantitative analysis of the weight; In frequency domain, the Fast Fourier Transform algorithm was used to calculate the spectrum within a deformation frequency area before and after the change of grids, from which the relationship between weight and spectrum was investigated. Two different equations evaluated by the above two methods were proposed in order to calculate the mass of an object. Both of them showed a high level of explanatory power of R^2 ($R^2=0.9833$ and $R^2=0.9698$, respectively). The equations were then used to determine the estimated mass. Estimated and measured values were plotted against each other. A high correlation ($R^2=0.9833$ and $R^2=0.9698$, respectively) was found between actual and calculated mass. Finally, Bland-Altman plot was introduced to access the agreement of the calculated mass and the actual mass. The average bias was -54.408g and -0.007g for spatial domain method and frequency domain method, respectively. Theoretical analysis and experiments were performed to verify the effectiveness of our approaches.

Keywords: thin plate spline; Fast Fourier Transform; mass; bending energy; image processing

1 Introduction

Generally, physical characteristics are the most important parameters in judging the quality of an object. The significant physical properties of an object are color, volume, mass, shape, size, etc. These properties can be estimated by using several sources of information. For instance, an object's size and shape can be judged based on visual as well as haptic cues. Though Ernst and Banks' research [1] indicated that human observers integrate visual and haptic size information in a statistically optimal fashion, in the sense that the integrated estimate is most reliable, it is hard for a computer to complete this because that means more sensors are required.

With the rapid development of robot and computer image vision technology, the image processing method makes it possible to identify and analyze the physical properties of an object, especially in agriculture [2–4] Xu et al. [5] used machine-vision technology to obtain shape, size, and color of strawberries and separate them into different grades. The correct percentages were 90%, 95%, 88.5% for each characteristic, respectively. M. Omid et al. [6] used two cameras to give perpendicular

views of the fruit and calculated their volumes by dividing the fruit image into a number of elementary elliptical frustums. The volumes computed showed good agreement with the actual volumes.

Although image processing approaches have been well developed for properties such as shape and volume measurement, applications to the analysis of the measurement of object mass are relatively rare. Current research on object mass measurement using image processing method mainly focuses on fruit mass measurement. A series of studies on the relationship between geometry and mass have been carried out for different fruit species. For example, for apples [7], mangos [8], apricots [9], and citrus fruits [6]. In these studies, weight of fruit was estimated by linear and non-linear models using different geometric characteristics such as minor diameter, area and volume. However, these approaches cannot evaluate the mass of an object with an irregular shape.

The objective of this study is to develop an image processing-based method which could estimate the mass of an object without considering its geometric characteristics. The experiments in this paper were conducted on a pair of images with grids on the tensile belt before and after the placement of weight sets. Our experimental results show that the method provides a valuable alternative to the traditional methods for the measurement of mass.

2 Theory

In this section, we give a background concerning the main theories of the thin plate spline and the Fourier transform.

2.1 Thin plate spline (TPS)

The thin plate spline is a transformation function which was first proposed by Duchon [10], and commonly used in image alignment and shape matching [11–13]. Nowadays, it's widely used in remote sensing, medical image analysis and pattern recognition [14–21].

Let (x_i, y_i) denote the coordinates of reference points in the plane, and v_i refers to the values of target function at the location (x_i, y_i) , with $i = 1, 2, \dots, n$.

In two-dimensional space, the bending energy functional of the thin-plate spline interpolation function is in the form of integral:

$$I(f) = \iint_{R^2} \left[\left(\frac{\partial^2 f}{\partial x^2} \right)^2 + 2 \left(\frac{\partial^2 f}{\partial x \partial y} \right)^2 + \left(\frac{\partial^2 f}{\partial y^2} \right)^2 \right] dx dy \quad (1)$$

The TPS interpolation function which minimizes $I(f)$ is given by

$$f(x, y) = a_1 + a_x x + a_y y + \sum_{i=1}^n w_i U(\|(x_i, y_i) - (x, y)\|) \quad (2)$$

Where $U(r_{ij}) = r_{ij}^2 \log r_{ij}^2$, $r_{ij} = (\|(x_i, y_i) - (x_j, y_j)\|)$. Note that $f(x, y)$ is divided into two parts: affine transformation parameterized by and non-affine warping specified by w . To make the $f(x, y)$ have square-integrable second derivatives, we have the following constraints:

$$\sum_{i=1}^n w_i = 0 \quad (3)$$

$$\sum_{i=1}^n w_i x_i = 0 \quad (4)$$

$$\sum_{i=1}^n w_i x_i = 0 \quad (5)$$

All together, these constraints are equivalent to the symmetric linear system of equations:

$$\begin{bmatrix} K & P \\ P^T & O \end{bmatrix} \begin{bmatrix} w \\ a \end{bmatrix} = \begin{bmatrix} v \\ o \end{bmatrix} \quad (6)$$

$$\text{Where } K = \begin{bmatrix} 0 & U(r_{12}) & \dots & U(r_{1n}) \\ U(r_{21}) & \dots & \dots & U(r_{2n}) \\ \dots & \dots & \dots & \dots \\ U(r_{n1}) & U(r_{n2}) & \dots & 0 \end{bmatrix}, n \times n; P = \begin{bmatrix} 1 & x_1 & y_1 \\ 1 & x_2 & y_2 \\ \dots & \dots & \dots \\ 1 & x_n & y_n \end{bmatrix}, n \times 3;$$

O denotes a 3×3 zero matrix, o is a 3×1 column vector of zeros, a refers to a column vector with element a_1, a_x, a_y and w, v , are vectors formed with w_i and v_i , respectively. For convenience, we will denote the $(n+3) \times (n+3)$ matrix of this system by L . And L_n^{-1} refers to the upper left $n \times n$ sub-block of L^{-1} , and then it can be shown that

$$I(f) \propto w K w^T = v (L_n^{-1} K L_N^{-1}) v^T \quad (7)$$

2.2 2-Dimensional Discrete Fourier Transform (2D-DFT)

The Discrete Fourier Transform (DFT) decomposes a function of time into the frequencies that make it up and plays an important role in various applications in signal processing and image processing. For example, image transformation [22–24], image reconstruction [25–27], image recognition [28–30], etc. In the image processing field, the Discrete Fourier transform study a signal in both time and frequency domains simultaneously, and the signal can be better understood through this way.

Let M and N be positive integers, the 2D-DFT of the function $f(x, y)$ can be calculated by

$$F(u, v) = \frac{1}{MN} \sum_{x=0}^{M-1} \sum_{y=0}^{N-1} f(x, y) e^{-j2\pi(\frac{ux}{M} + \frac{vy}{N})} \quad (8)$$

Returning the Fourier spectrum $F(u, v)$ at the frequencies u and v for $u = 1, 2, \dots, M-1$ and $v = 1, 2, \dots, N-1$. Combined with Euler's formula, the Fourier transform can be generally rewrote in the form of a real and an imaginary parts as:

$$F(u, v) = a(u, v) - ib(u, v) \quad (9)$$

Where a and b are the Fourier coefficients at the frequencies u and v . The power spectrum is then estimated by:

$$E(u, v) = a^2(u, v) + b^2(u, v) \quad (10)$$

And the logarithmic power spectrum can be defined as

$$P(u, v) = \log E(u, v) \quad (11)$$

to avoid the result of $P(u, v)$ being a negative value, we add a correction parameter C (C is a positive integer), then the corrected power spectrum can be calculated by

$$P(u, v) = P(u, v) + C \quad (12)$$

In our study, the value of C is 100. Since it is a very time-consuming task to calculate DFT directly, DFT is computed efficiently with Fast Fourier transform (FFT) [31] in this paper. Fast Fourier transform can be regarded as a fast version of DFT expressed by the formula

$$\begin{aligned} F(u) &= \frac{1}{2M} \sum_{x=0}^{2M-1} f(x)W_{2M}^{ux} \\ &= \frac{1}{2} \left\{ \frac{1}{M} \sum_{x=0}^{M-1} f(2x)W_{2M}^{u(2x)} + \frac{1}{M} \sum_{x=0}^{M-1} f(2x+1)W_{2M}^{u(2x+1)} \right\} \end{aligned} \quad (13)$$

Where $u = 1, 2, \dots, M - 1$.

3 Materials and methods

In this paper, our proposed method includes several components: data acquisition, Feature calculation by image processing, determination of correlation formula, and computation of estimated mass. These steps are further elaborated in the following sub-sections. Figure 1 summarizes the procedures involved.

Figure 1 Flowchart of the mass measuring system

3.1 Data acquisition

The required materials mainly include a tensile belt with good elasticity, a camera, a red pen, a series of weights with different values. First, we use a red pen to draw a series of uniform red dots on the central area of the tensile belt. Next, fix a small iron stick on the tensile belt with needlework and tie a string of a certain length below it to hang weights. Figure 2 shows the treated tensile belt. The role of the iron stick is to make sure that tensile belt will not wrinkle during the stretching process because only one point is stressed. Finally, a thumbtack is used to fix the tensile belt to a test bench with a certain height. After placing the camera in a fixed position and adjusting the shooting angle, images of tensile belt are captured by the camera in 512×512 pixels and stored on the PC for further analysis. Figure 3 shows the deformation process of the tensile belt with different weights.

Figure 2 Treated tensile belt

Figure 3 Deformation process of tensile belt with different weights

3.2 Feature calculation

The image processing aspect of this study consists of two parts: spatial domain analysis and frequency domain analysis. In both experiments, the original images are resized to the same size in 256×256 pixels.

In spatial domain experiment, the coordinates of the marker points on images are recorded manually, where the coordinates of the marker points in the 0g image is denoted as p , and p' is the coordinates of the marker points corresponding to other weights. Our algorithm written in Matlab 2014a is developed for calculating the bending energy based on TPS algorithm. Entering the values of p and p' into the program will generate the corresponding values of bending energy.

In frequency domain experiment, background segmentation is firstly undertaken in order to eliminate the impact of background on results. Initially, an image of the background (tensile belt without marker points) is captured, from which the standard deviation values (denoted as σ) of the image can be calculated and saved in a database by determining the R, G and B values of all of the pixels in the background image. Then the R, G and B values of all the pixels in the marker point image are found and compared with those of the background image. If the difference between the two sets of R, G and B values are higher than 2σ , then the pixel will be regarded as marker point, else background. The marker point image after segmentation is finally inputted into the program to calculate the power spectrum.

The necessity of the background segmentation procedure is indicated in Fig.4: Figure 4a and 4c show the power spectrum images with different weights before background segmentation. The images in Fig. 4b and 4d represent the result of the FFT algorithm after the background removal procedure (using the 2σ difference between the two RGB values of foreground and background color). This experiment clearly demonstrates the improvement of the spectrum image quality after the background segmentation procedure, and the value of power spectrum is calculated within a red circle region which has been proven to have the largest change with grid deformation [32].

Figure 4 Power spectrum images before and after background removal. (a) power spectrum image with 0g weight before background removal; (b) power spectrum image with 0g weight after background removal; (c) power spectrum image with 300g weight before background removal; (d) power spectrum image with 300g weight after background removal.

3.3 Statistical analysis

To validate the effectiveness of the proposed image processing methods, initially, the bending energy values and power spectrum values corresponding to different weights are recorded as illustrated in Table 1 and 2. Specifically, to decrease the spectrum spreading effect, the area is chosen as the red circles with radius of 3 unit pixels in Fig. 4b and 4d, where the center point is located at the maximum spectrum point with 0g weight, and the final frequency feature is the sum of the

power spectrum values in this area. In order to reduce unexpected error, both of the experiments have been undertaken for ten times to calculate the average of experimental values as the final result.

The correlations between weight and bending energy, weight and power spectrum can be obtained through the scatter plot. According to the linear relation from the experiments, we can calculate the value of mass. Finally, the Bland–Altman approach [33] is used to plot the agreement between the calculated and measured mass.

Table 1 Weight vs. Bending energy in spatial domain

Weight g	Bending energy	Weight g	Bending energy	Weight g	Bending energy
50	0.0675315	750	0.2534495	1450	0.4961905
100	0.1070425	800	0.283556	1500	0.560845
150	0.118597	850	0.3168385	1550	0.554938
200	0.126451	900	0.302148	1600	0.5109105
250	0.1445605	950	0.3099495	1650	0.5887875
300	0.146704	1000	0.388668	1700	0.59523
350	0.1698135	1050	0.386446	1750	0.5883385
400	0.170027	1100	0.3481495	1800	0.636557
450	0.1838315	1150	0.452999	1850	0.624865
500	0.2013185	1200	0.4190905	1900	0.653381
550	0.208804	1250	0.4549565	1950	0.6426465
600	0.2253255	1300	0.490571	2000	0.7339365
650	0.2340425	1350	0.4452105		
700	0.290691	1400	0.4634985		

Table 2 Weight vs. Power spectrum in frequency domain

Weight g	Power spectrum	Weight g	Power spectrum
0	1096.37	170	598.97
10	1066.23	180	622.73
20	1051.38	190	521.32
30	1030.35	200	523.57
40	1024.39	210	471.56
50	1000.26	220	385.49
60	932.4	230	464.31
70	895.35	240	323.56
80	861.77	250	213.09
90	882.36	260	216.91
100	876.52	270	89.21
120	799.64	280	74.27
130	747.95	290	35.1
140	742.01	300	25.27
150	648.28	350	0
160	616.99		

4 Results and Discussion

The correlations between weight and bending energy, weight and power spectrum are shown in Fig. 5 and Fig. 6, respectively. Figure 5 presents that the TPS

Figure 5 Experimental data distribution in the spatial domain (0–2000 g in increments of 50 g)

minimum bending energy value increases as the mass of weights on tensile belt increases, while Fig. 6 shows that the power spectrum value decreases as the weights

Figure 6 Experimental data distribution in the frequency domain (0–350 g in increments of 10 g)

on tensile belt increases. The experimental results are consistent with our expected conjecture. Accordingly, the following correlation formulas, derived based on the collected data on mass and computed bending energy and power spectrum by image processing methods were obtained:

$$\text{Bending energy} = 0.0003\text{Mass} + 0.0486$$

$$\text{Power spectrum} = -3.5565\text{Mass} + 1168.7$$

The results of comparison between predicted (spatial domain and frequency domain) and actual mass of weights are shown in Fig. 7 and 8, respectively. The coefficient of determination (R^2) for spatial domain method and frequency domain method were 0.9833, and 0.9698. The R^2 values can be interpreted as the proportion of the variance in the image processing estimated attributable to the variance in the actual measurements. The higher the R^2 values, the closer the image processing results are to the actual results. The proposed image processing methods yielded above 96% accuracy in estimating weights mass.

Figure 7 Comparison of predicted and actual mass with spatial domain method

Figure 8 Comparison of predicted and actual mass with frequency domain method

Finally, the Bland-Altman plot is introduced to assess the agreement of the image processing methods and the traditional method. In these figures, the dash lines indicate the 95% limits of agreement while the solid lines show the average difference. The Bland-Altman plot for comparison of mass computed by spatial domain method and measured with balance is shown in Fig. 9. The result shows agreement with the 95% limits of agreement being -222.888 to $+114.071$ g and the average bias is -54.408 g. The Bland-Altman plot for frequency domain method versus the traditional method is shown in Fig. 10, showing that excellent agreement with the 95% limits of agreement being -33.715 to $+33.701$ g and the average bias is -0.007 g.

Figure 9 Bland-Altman plot for spatial domain method versus the traditional method

Figure 10 Bland-Altman plot for frequency domain method versus the traditional method

5 Conclusions

In this paper, two image processing techniques for estimating the mass of an object were presented and discussed. In the spatial domain and frequency domain experiments, thin plate spline algorithm and FFT algorithm were adopted to analyze the

images with grid points respectively. The spatial domain experiment uses the manual acquisition of experimental raw data, while the frequency domain experiment uses the automatic acquisition of experimental raw data. The experimental results showed that the mass of an object is linearly proportional to the minimum bending energy value of TPS while is inversely proportional to the sum of the spectral values of the central region of the FFT spectrogram. In summary, the results obtained in two different ways are ultimately consistent with the theoretical predictions, and mass is able to be measured efficiently by image processing methods.

Abbreviations

TPS: Thin plate spline; 2D-DFT: 2-Dimensional Discrete Fourier Transform; DFT: Discrete Fourier Transform; FFT: Fast Fourier transform

Availability of data and materials

Not applicable.

Competing interests

The authors declare that they have no competing interests.

Funding

This work is supported by the National Natural Science Foundation of China (Grants Nos. 81460274 and 81760324); and Natural Science Foundation of Guangxi (Grant No. 2017JJA170765y).

Author's contributions

All authors contributed equally in this work. The authors read and approved the final manuscript.

Acknowledgements

Not applicable.

Author details

¹School of Computer, Electronics and Information, Guangxi University, Nanning, 530004 Guangxi, China. ²Guangxi Key Laboratory of Multimedia Communications and Network Technology, Nanning, Guangxi, China. ³College of Medical, Guangxi University, Nanning, Guangxi, China. ⁴Guangxi Big White and Little Black Robots Co, Ltd, Nanning, Guangxi, China.

References

- Ernst, M.O., Banks, M.S.: Humans integrate visual and haptic information in a statistically optimal fashion. *Nature* **415**(6870), 429–433 (2002)
- Chen, Y.R., Chao, K., Kim, M.S.: Machine vision technology for agricultural applications. *Computers and Electronics in Agriculture* **36**(2-3), 173–191 (2002)
- Chong, V.K., Kondo, N., Ninomiya, K., Nishi, T., Monta, M., Namba, K., Zhang, Q.: Features extraction for eggplant fruit grading system using machine vision. *Applied Engineering in Agriculture* **24**(5), 675–684 (2008)
- Cubero, S., Lee, W.S., Aleixos, N., Albert, F., Blasco, J.: Automated systems based on machine vision for inspecting citrus fruits from the field to postharvest—a review. *Food and Bioprocess Technology* **9**(10), 1623–1639 (2016)
- Xu, L., Zhao, Y.: Automated strawberry grading system based on image processing. *Computers and Electronics in Agriculture* **71**(supp-S1), 32–39 (2010)
- Omid, M., Khojastehnazhand, M., Tabatabaeefar, A.: Estimating volume and mass of citrus fruits by image processing technique. *Journal of Food Engineering* **99**(2), 315–321 (2010)
- Tabatabaeefar, A., Rajabipour, A.: Modeling the mass of apples by geometrical attributes. *entia Horticulturae* **105**(3), 373–382 (2005)
- Momin, M.A., Rahman, M.T., Sultana, M.S., Igathinathane, C., Ziauddin, A.T.M., Grift, T.E.: Geometry-based mass grading of mango fruits using image processing. *Information Processing in Agriculture* **4**(2) (2017)
- Naderi-Boldaji, M., Fattahi, R., Ghasemi-Varnamkhashti, M., Tabatabaeefar, A., Jannatizadeh, A.: Models for predicting the mass of apricot fruits by geometrical attributes (cv. shams, nakhjavan, and jahangiri). *entia Horticulturae* **118**(4), 293–298 (2008)
- Duchon, J.: Splines minimizing rotation-invariant semi-norms in sobolev spaces. *Constructive Theory of Functions of Several Variables* **571** (1977)
- Lu, X., Jain, A.K.: Deformation modeling for robust 3d face matching. In: 2006 IEEE Computer Society Conference on Computer Vision and Pattern Recognition, pp. 1346–1357 (2008)
- Ross, A., Nadgir, R.: A thin-plate spline calibration model for fingerprint sensor interoperability. *IEEE Transactions on Knowledge and Data Engineering* **20**(8), 1097–1110 (2008)
- Yang, J., Williams, J.P., Sun, Y., Blum, R.S., Xu, C.: A robust hybrid method for nonrigid image registration. *Pattern Recognition* **44**(4), 764–776 (2011)
- Goshtasby, A.: Registration of images with geometric distortions. *IEEE Trans.geo.remote Sensing* **26**(1), 60–64 (1988)
- Bentoutou, Youcef, Taleb, Nasreddine, Kpalma, Kidiyo, Ronsin, Joseph: An automatic image registration for applications in remote sensing. *IEEE Transactions on Geoscience and Remote Sensing* (2005)

16. Ma, J., Zhou, H., Zhao, J., Gao, Y., Jiang, J., Tian, J.: Robust feature matching for remote sensing image registration via locally linear transforming. *IEEE Transactions on Geoscience and Remote Sensing* **53**(12), 6469–6481 (2015)
17. Bookstein, F.L.: Principal warps: thin-plate splines and the decomposition of deformations. *IEEE Transactions on Pattern Analysis and Machine Intelligence* **11**(6), 567–585 (2002)
18. Bazen, A.M., Gerez, S.H.: Fingerprint matching by thin-plate spline modelling of elastic deformations. *Pattern Recognition* **36**(8), 1859–1867 (2003)
19. Wang, H., Zheng, B., Good, W., Zhuang, T.G.: Thin-plate spline based automatic alignment of dynamic mr breast images. In: International Conference of the IEEE Engineering in Medicine and Biology Society (2000)
20. Qiu, Z., Tang, H., Tian, D.: Non-rigid medical image registration based on the thin-plate spline algorithm. *Computer Simulation* **27**(6), 275–278 (2009)
21. Mitra, J., Oliver, A., Marti, R., Lladó, X., Vilanova, J.C., Meriaudeau, F.: A thin-plate spline based multimodal prostate registration with optimal correspondences. In: International Conference on Signal-Image Technology and Internet-Based Systems (2010)
22. Pun, C.M.: A novel dft-based digital watermarking system for images. In: International Conference on Signal Processing (2007)
23. Solachidis, V., Pitas, L.: Circularly symmetric watermark embedding in 2-d dft domain. *IEEE Trans Image Process* **10**(11), 1741–1753 (2001)
24. Barni, M., Bartolini, F., De Rosa, A., Piva, A.: A new decoder for the optimum recovery of nonadditive watermarks. *IEEE Trans Image Process* **10**(5), 755–66 (2001)
25. Sumanaweera, T., Liu, D.: Medical image reconstruction with the fft. *Gpu Gems* (3), 3019–3025 (2005)
26. Wan, X.-f., Yang, Y.: Super-resolution image reconstruction. In: International Conference on Computer Application and System Modeling (2010)
27. Ghorbel, F., Derrode, S., Mezhoud, R., Bannour, T., Dhahbi, S.: Image reconstruction from a complete set of similarity invariants extracted from complex moments. *Pattern Recognition Letters* **27**(12), 1361–1369 (2006)
28. Ito, K., Morita, A., Aoki, T., Higuchi, T., Nakajima, H.: A fingerprint recognition algorithm using phase-based image matching for low-quality fingerprints. In: IEEE International Conference on Image Processing (2005)
29. Miyazawa, K., Ito, K., Aoki, T., Kobayashi, K., Nakajima, H.: An effective approach for iris recognition using phase-based image matching. *IEEE Transactions on Pattern Analysis and Machine Intelligence* **30**(10), 1741–56 (2008)
30. Ito, K., Aoki, T., Nakajima, H., Kobayashi, K., Higuchi, T.: A palmprint recognition algorithm using phase-based image matching. In: International Conference on Image Processing (2009)
31. Sorensen, H., Jones, D., Heideman, M., Burrus, C.: Real-valued fast fourier transform algorithms. *IEEE Transactions on Acoustics Speech and Signal Processing* **35**(6), 849–863 (1987)
32. Xuejun, Z., Xiangrong, Z., Takeshi, H., Hiroshi, F.: Non-invasive assessment of hepatic fibrosis by elastic measurement of liver using magnetic resonance tagging images. *Applied Sciences* **8**(3), 437 (2018)
33. Altman, B.D.G.: Statistical methods for assessing agreement between two methods of clinical measurement. *International Journal of Nursing Studies* (2010)

Figures

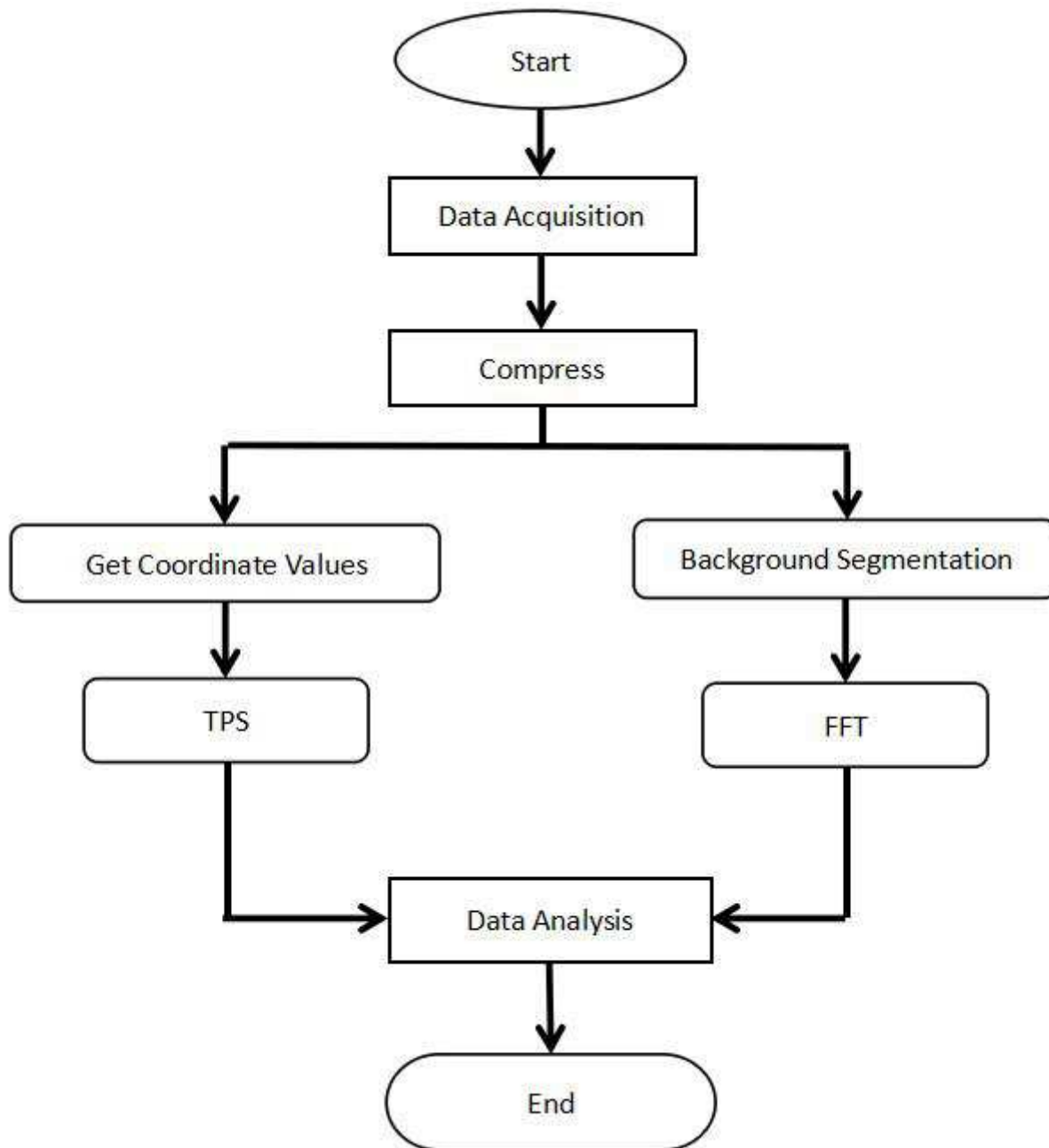


Figure 1

Flowchart of the mass measuring system

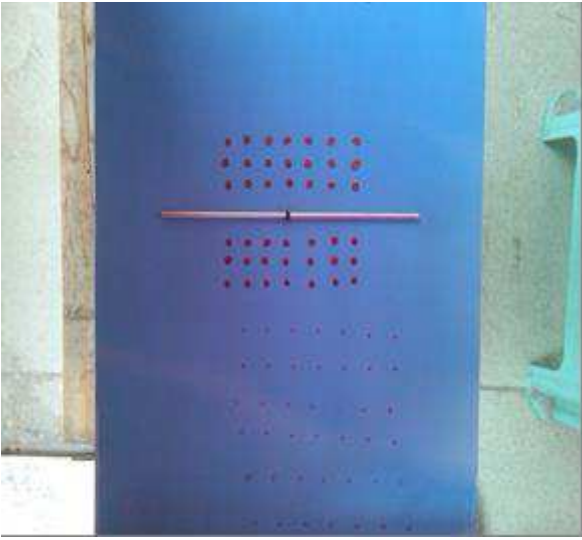
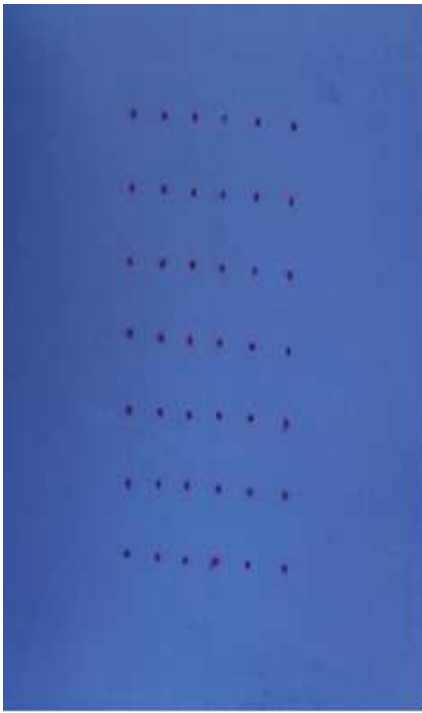
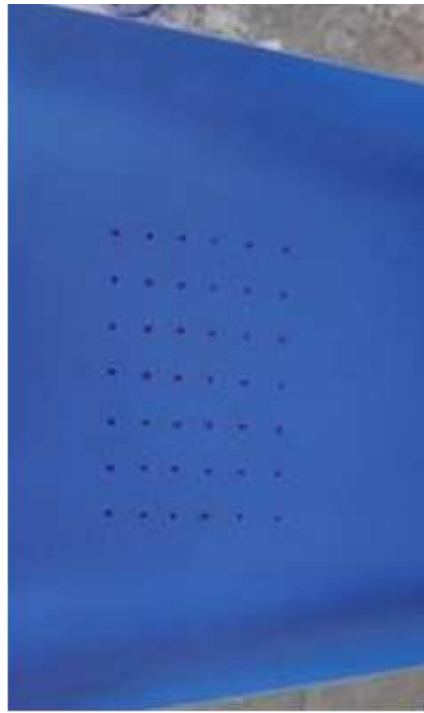


Figure 2

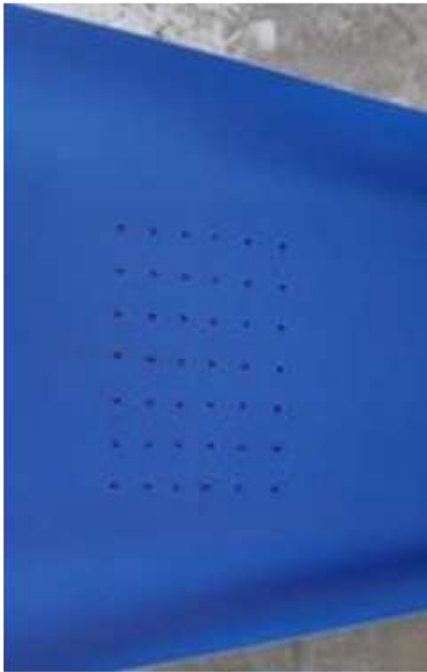
Treated tensile belt



(a) 0g



(b) 550g



(c) 1200g



(d) 2000g

Figure 3

Deformation process of tensile belt with different weights

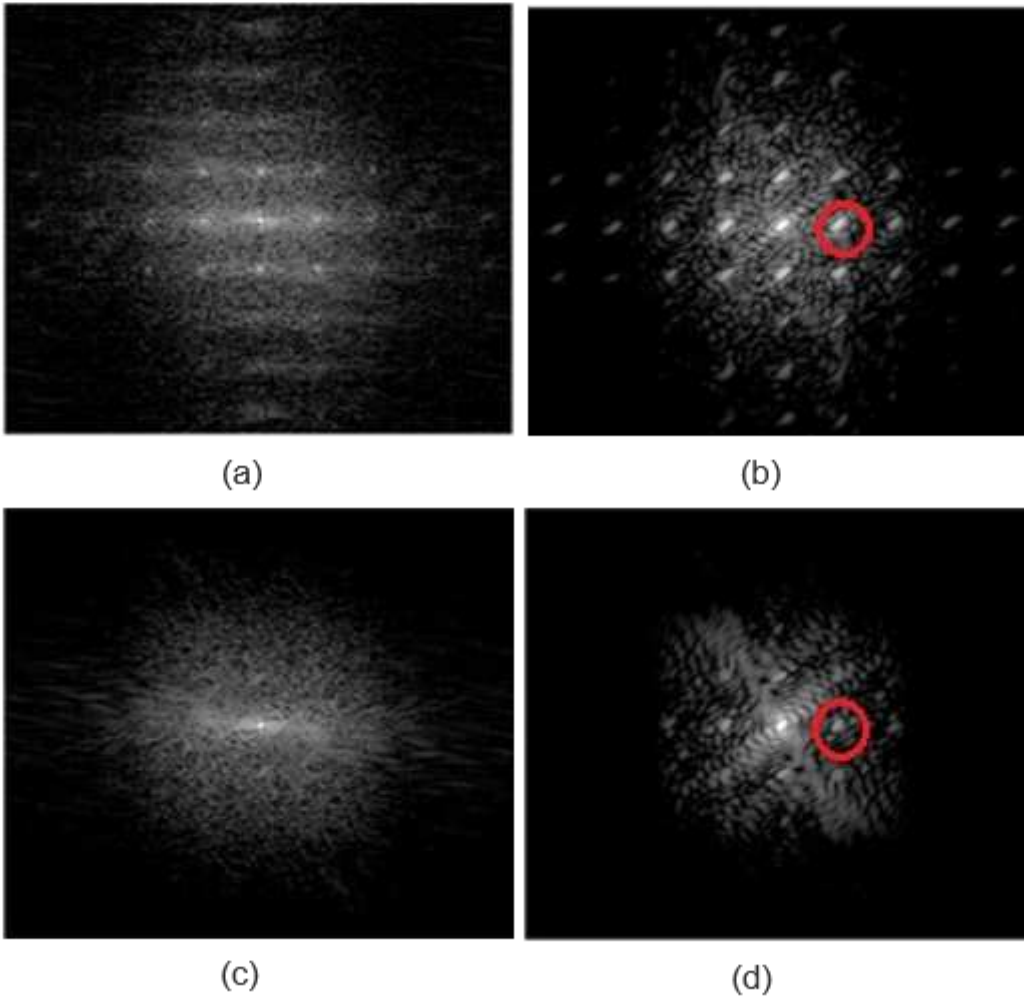


Figure 4

Power spectrum images before and after background removal. (a) power spectrum image with 0g weight before background removal; (b) power spectrum image with 0g weight after background removal; (c) power spectrum image with 300g weight before background removal; (d) power spectrum image with 300g weight after background removal.

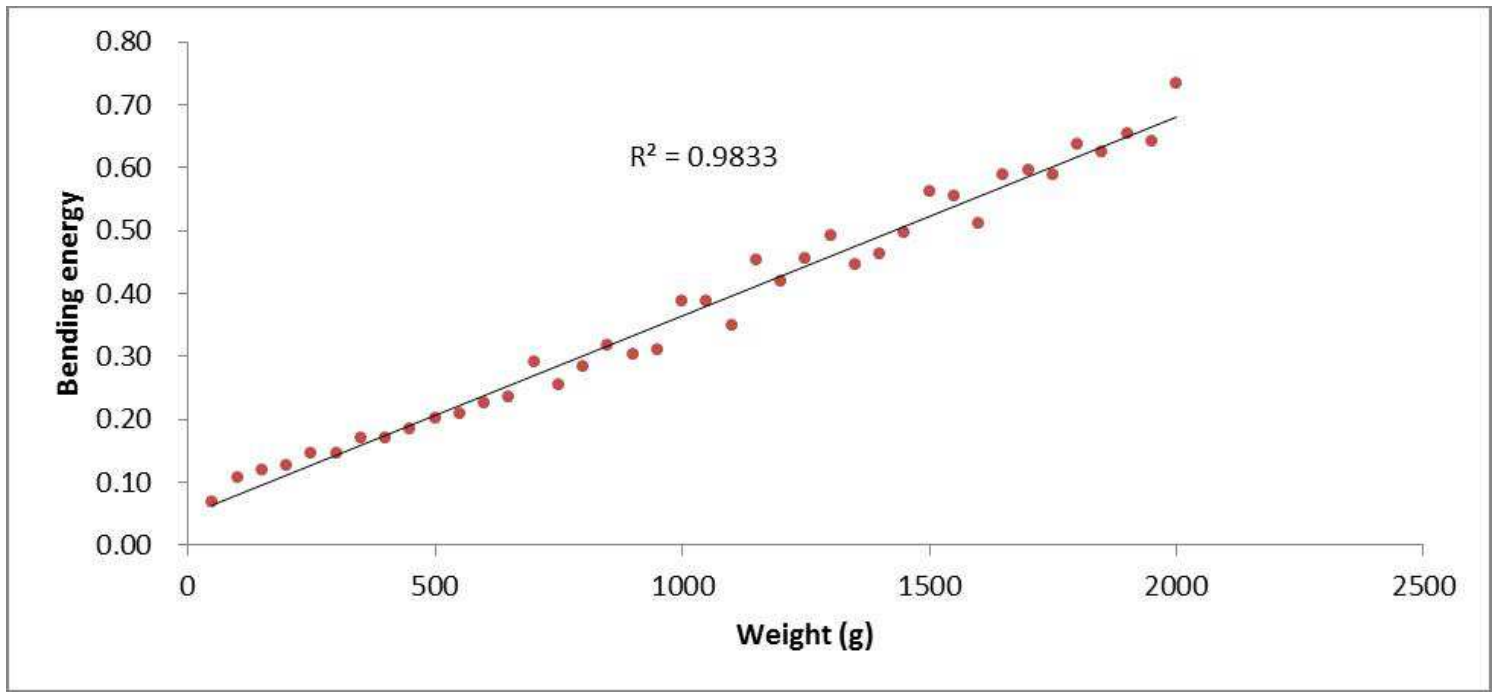


Figure 5

Experimental data distribution in the spatial domain (0 2 000 g in increments of 50 g)

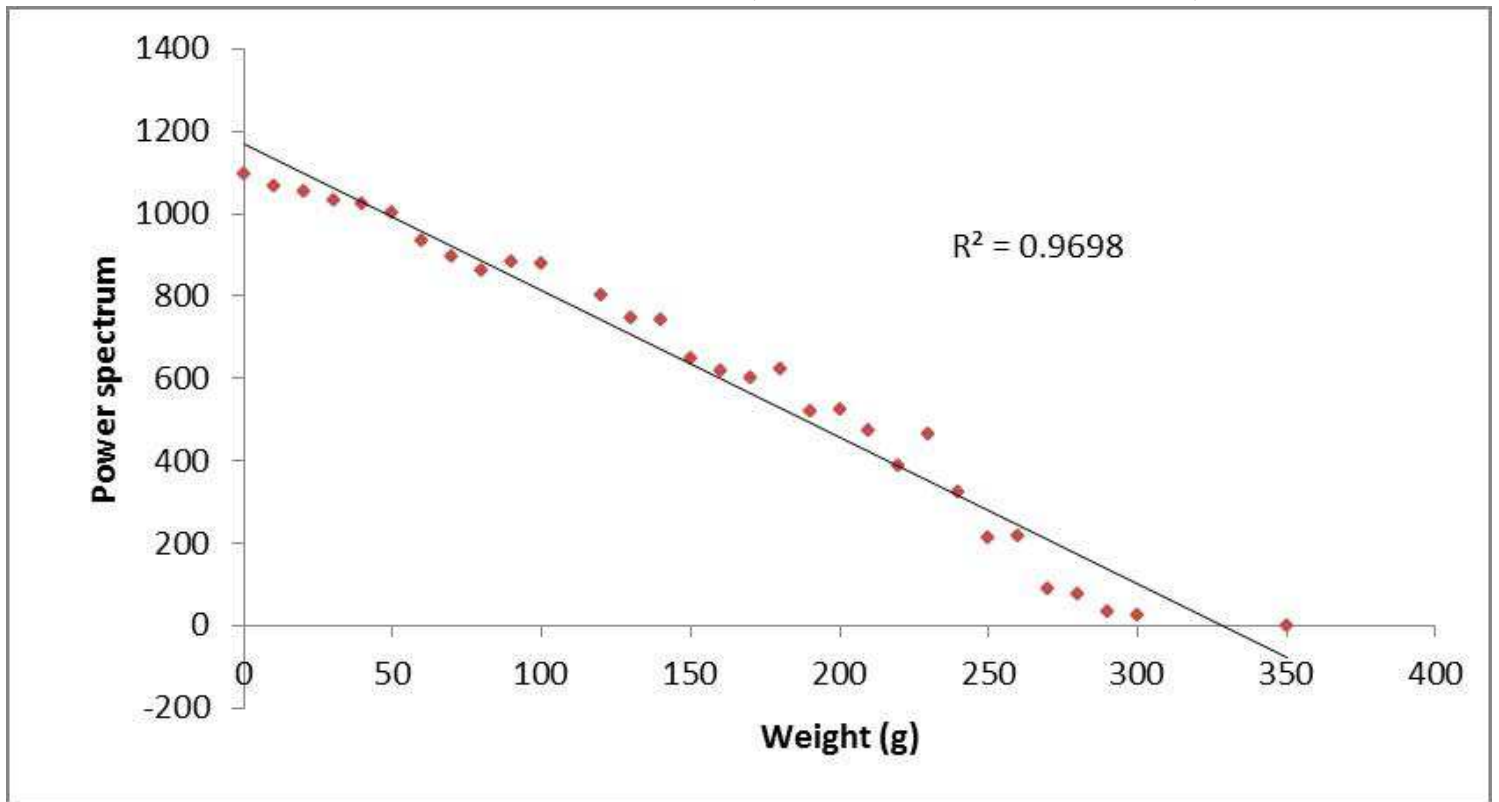


Figure 6

Experimental data distribution in the frequency domain (0 350 g in increments of 10 g)

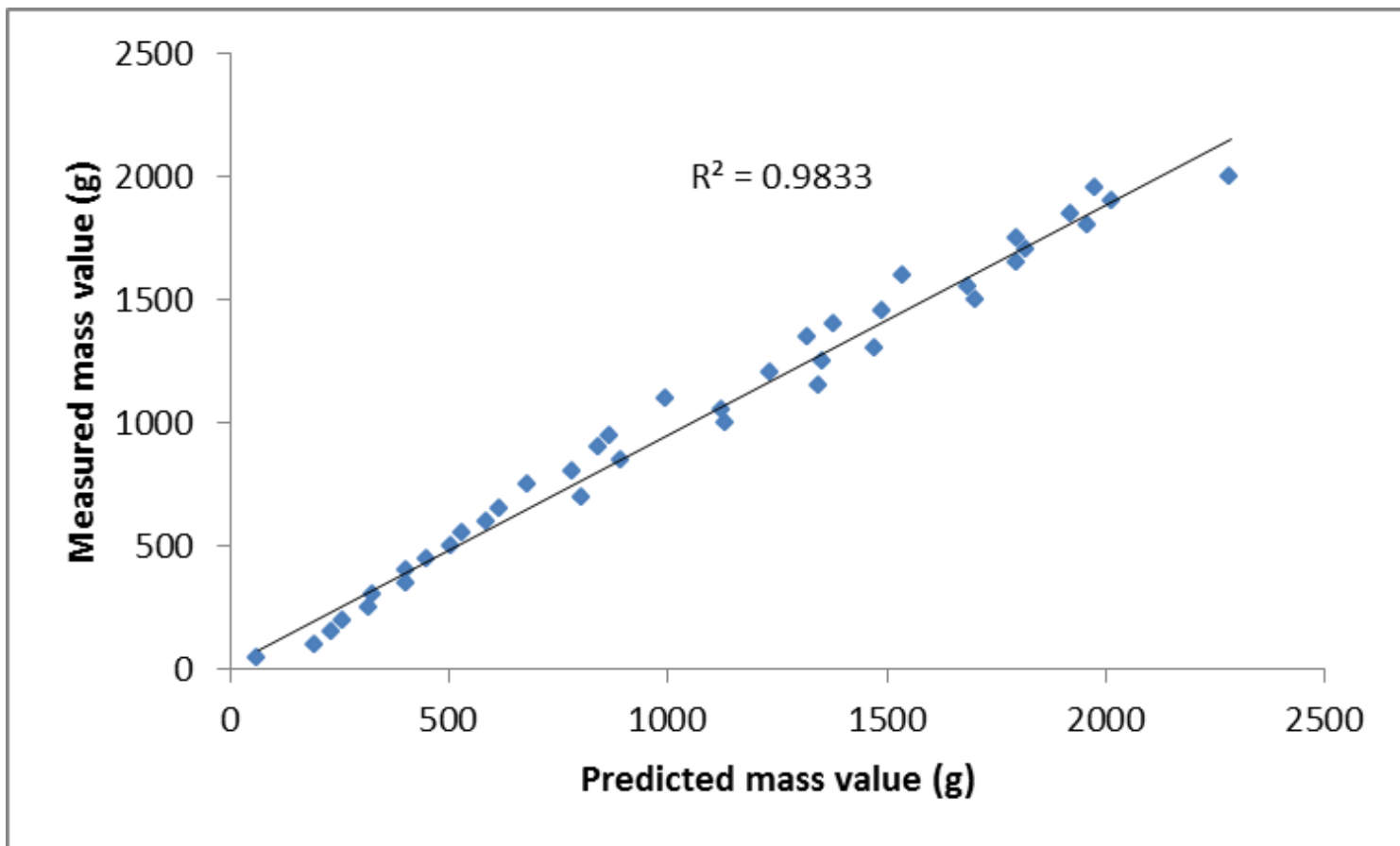


Figure 7

Comparison of predicted and actual mass with spatial domain method

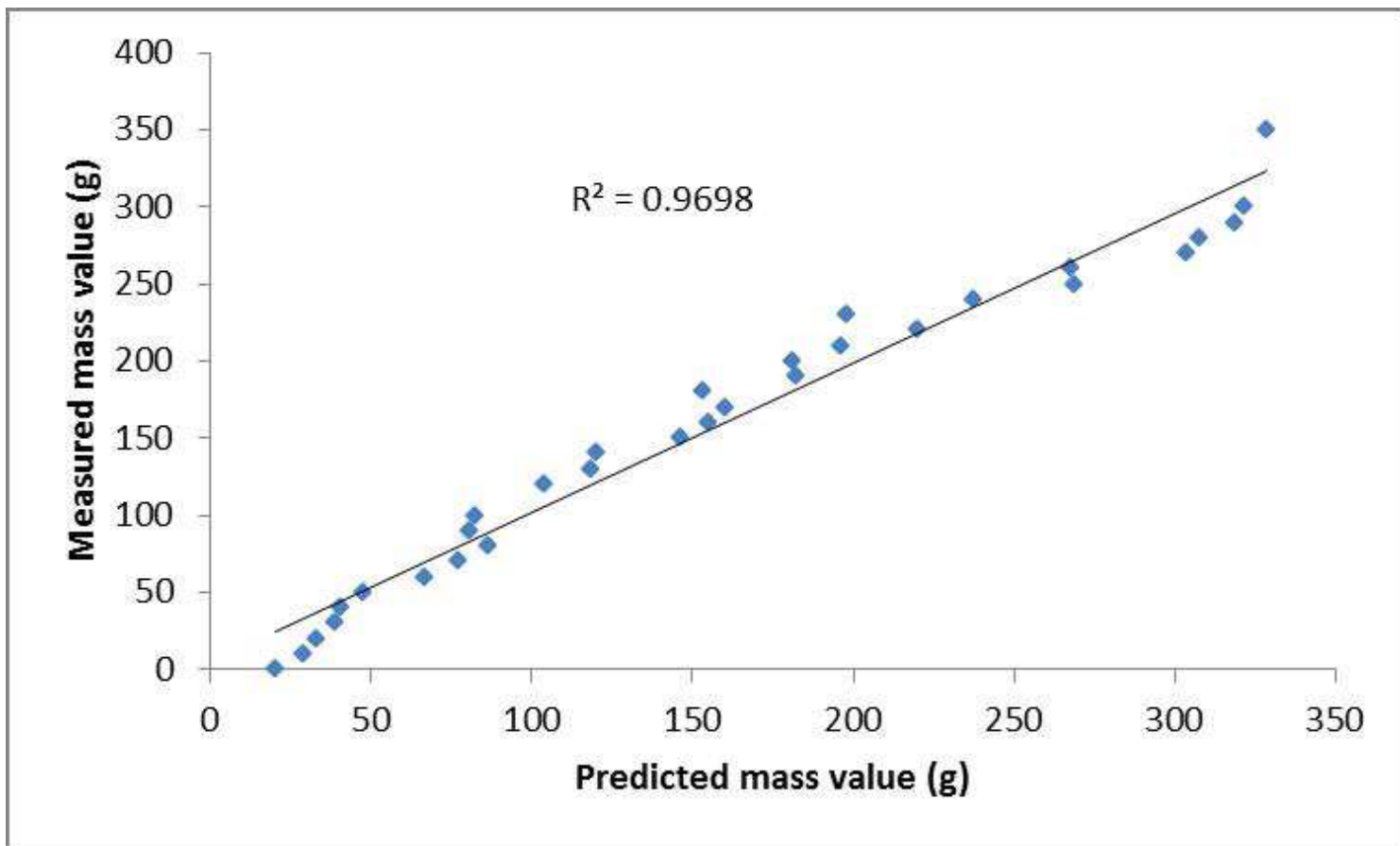


Figure 8

Comparison of predicted and actual mass with frequency domain method

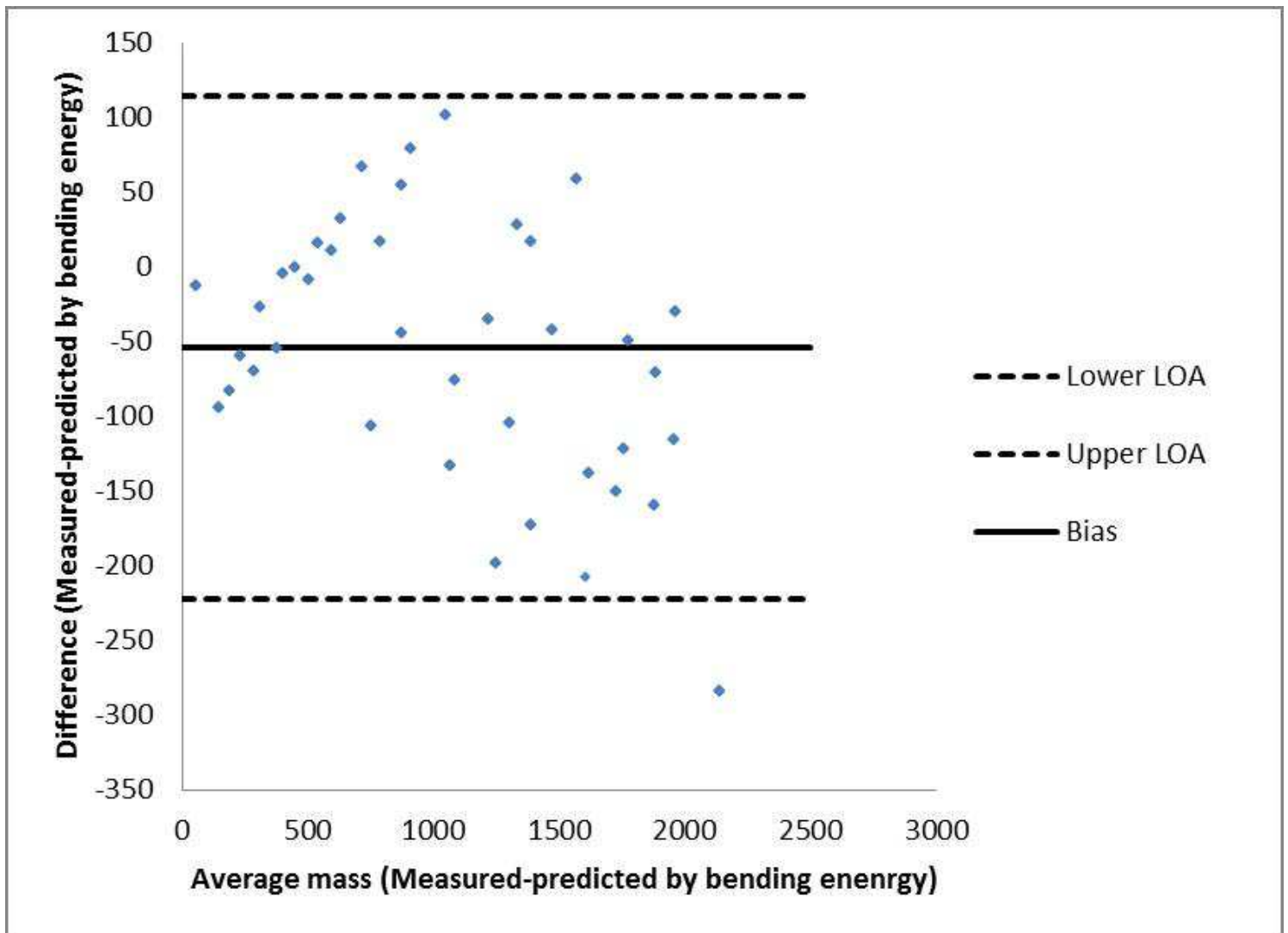


Figure 9

Bland-Altman plot for spatial domain method versus the traditional method

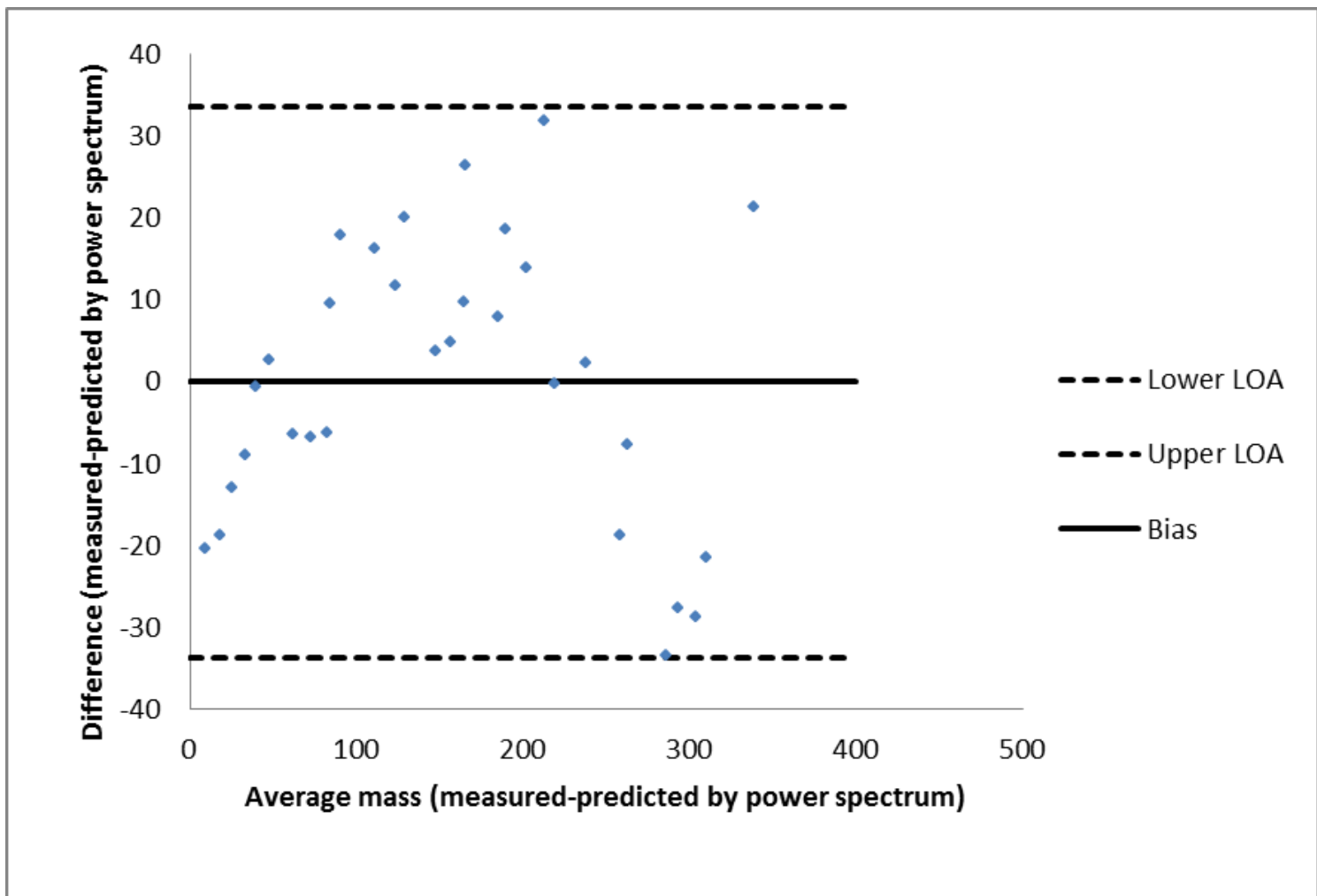


Figure 10

Bland-Altman plot for frequency domain method versus the traditional method